International Journal of Scientific Research in Science, Engineering and Technology

Print ISSN - 2395-1990
Online ISSN : 2394-4099

OPEN ACCESS

Available Online at :www.ijsrset.com
doi : https://doi.org/10.32628/IJSRSET2411432

In-Silico Design and Optimization of p-$BaSi_2$/n-Bi_2S_3 Heterojunction for Enhanced Photovoltaic Performance

Saksham Mathur

Anand Niketan International School, Satellite Campus, Ahmedabad, Gujarat, India

E-mail: aaravarchi0911@gmail.com

ARTICLEINFO

Article History:

Accepted: 12 Oct 2024
Published: 28 Oct 2024

Publication Issue :
Volume 11, Issue 5
Sept-Oct-2024

Page Number :
293-305

ABSTRACT

This study aims to explore the integration of Bi_2S_3 as an electron transport layer (ETL) in $BaSi_2$-based thin-film solar cells for the enhanced performance. Using the globally accepted SCAPS-1D simulation tool, a novel device architecture consisting of Al/SnO_2:F/Bi_2S_3/$BaSi_2$/Ni was systematically designed and optimized. Key optimization parameters include the thicknesses, carrier concentrations, bulk defect densities of each layer, interface defects, operating temperature, and the influence of series and shunt resistance on overall efficiency. The simulation results reveal that a $BaSi_2$ layer with an optimized thickness of 1 μm and a doping concentration of 5 x 10^{19} cm^{-3}, yields noteworthy outcomes. Specifically, champion efficiency (η) of 26.56% along with an open-circuit voltage (Voc) of 1.00 V, a short-circuit current (Jsc) of 32.74 mA/cm^2, and a fill factor of 80.65%. These findings highlight the potential of p-$BaSi_2$/n-Bi_2S_3 heterojunction solar cells to achieve high efficiency through careful optimization of material and device parameters, offering a promising approach for next-generation thin-film photovoltaic applications.

Keywords : $BaSi_2$, Bi_2S_3 ETL, Thin film solar cell, SCAPS-1D, Optimization, Simulation

I. INTRODUCTION

The surge in demand for renewable energy sources has positioned photovoltaic technology at the forefront of sustainable energy solutions. Solar energy, in particular, has garnered significant attention due to its potential to provide clean and abundant power. Currently, wafer-based silicon solar cells dominate the market, capturing approximately 80-90% of the global share [1-4]. This prevalence is largely attributed to the abundance of silicon on Earth and the advanced technologies developed for its fabrication. However, despite their widespread use, there are inherent limitations associated with silicon solar cells that prompt the exploration of alternative materials and technologies.

In recent years, thin-film solar cell technologies have gained substantial attention as promising alternatives to conventional wafer-based silicon cells. Thin-film materials such as Copper Indium Gallium Selenide (CIGS) and Cadmium Telluride (CdTe), have emerged as promising contenders in the photovoltaic landscape. These materials are particularly appealing due to their cost-effective growth procedures and high optical absorption capabilities. However, the reliance on rare elements like indium (In) and tellurium (Te) in CIGS and CdTe poses significant challenges for large-scale deployment, particularly at terawatt levels [5]. In parallel, silicon based thin-film solar cells have also been extensively studied to address the material usage concerns of wafer-based silicon cells and to enhance efficiency through innovative light-trapping systems [6]. Nevertheless, achieving efficiencies exceeding 20% remains a formidable challenge [6].

This quest for improved performance has catalysed interest in novel semiconducting materials suitable for thin-film photovoltaic applications. Among these candidates, barium disilicide ($BaSi_2$) has emerged as a material with considerable potential. Theoretical and Experimental studies indicate that orthorhombic $BaSi_2$ possesses a band gap of approximately 1.3 eV [7] and exhibits high absorption coefficients exceeding 3×10^4 cm^{-1} [8-10]. Recent experimental findings have also highlighted $BaSi_2$'s favourable minority-carrier properties, including a diffusion length (L = 10 μm) [11] and long minority-carrier lifetimes (τ = 10 μs) [12], which are critical for efficient charge transport and collection in photovoltaic devices. Furthermore, potential variations around grain boundaries (GBs) have been shown to enhance carrier collection, thereby reducing recombination losses [13]. These characteristics suggest that $BaSi_2$ could serve as a viable candidate for next-generation thin-film solar cells.

Recent literature underscores the advancements made in $BaSi_2$-based solar cell devices. Experimental investigations have reported efficiencies of 9% and 10% for p-$BaSi_2$ on Si(111) substrates and $BaSi_2$/c-Si heterojunction solar cells fabricated via Molecular Beam Epitaxy (MBE) [14,15]. Theoretical models have projected even higher efficiencies; for instance, n^+-$BaSi_2$/p-$BaSi_2$ and p^+-$BaSi_2$/n-$BaSi_2$ homojunction solar cells have achieved efficiencies of up to 22.5% with a 2 μm thick absorber layer [16]. Additionally, simulations have suggested potential efficiencies reaching 28% for double-junction perovskite/$BaSi_2$ structures with absorber thicknesses below 2 μm [17]. Furthermore, numerical optimization studies have indicated maximum efficiencies of 24.12% and 25.28% for $BaSi_2$ Schottky-junction solar cells under varying doping conditions [18].

Despite these promising results, it is essential to recognize that high absorber layer thickness can lead to increased recombination losses and elevated series resistance within the devices. Thicker layers necessitate more material, which not only increases the risk of defects but also complicates efficient charge transport—factors that can adversely affect overall device performance.

To address these challenges, recent research has focused on reducing absorber layer thickness while maintaining or enhancing efficiency levels. For instance, MMA Moon et al. [19] simulated an Al/SnO:F/CdS/$BaSi_2$:B/Cu configuration that yielded a theoretical efficiency of 26.32% with an absorber layer thickness of just 1.2 μm. However, the use of CdS as an electron transport layer (ETL) raises environmental concerns due to its toxicity, prompting researchers to seek alternative materials that can deliver comparable physical and optoelectronic properties without the associated risks.

In this context, MF Rahman et al. [20] explored configurations utilizing three different wide-bandgap S-chalcogenides—Zn(O,S), SnS_2, and WS_2—as ETLs in place of CdS. Their findings revealed efficiencies of

17%, 17.1%, and 22.2%, respectively; however, these performances fell short of expectations largely due to unfavourable conduction band offsets (CBOs) of -1.00 eV (Zn(O,S)), -0.96 eV (SnS_2), and -0.65 eV (WS_2) [20]. These large negative CBO values create potential barriers that hinder efficient electron transport, leading to significant performance losses.

To address these issues effectively, it is imperative to identify ETLs that exhibit optimal band alignment and facilitate efficient carrier transport within the device architecture. In this regard, bismuth sulfide (Bi_2S_3) presents itself as a compelling candidate for use as an ETL due to its advantageous properties [21]. In particular, a high absorption coefficient (> 10^4 cm^{-1} for λ < 780 nm and exceeding 10^5 cm^{-1} for λ < 500 nm) [21], along with its notable electron mobility of 28 cm^2 $V^{-1}s^{-1}$ [21]. Additionally, Bi_2S_3 is environmentally friendly and can be synthesized at low temperatures in ambient conditions [21].

Conventional ETLs such as zinc oxide (ZnO) and titanium dioxide (TiO_2) typically require high annealing temperatures (>300 °C) to achieve high-quality thin films [21-23]; however, Bi_2S_3 can be synthesized at room temperature through simple solution processes [21]. Various deposition techniques—such as spray pyrolysis, electrodeposition, vacuum thermal evaporation, chemical bath deposition, and ionic layer adsorption—have been employed to fabricate Bi_2S_3 thin films with reported band gap values ranging from 1.52 eV to 1.9 eV depending on the method used [24].

In light of these advantages, the present study aims to explore the use of Bi_2S_3 as an ETL in $BaSi_2$-based thin-film solar cells. Utilizing the globally accepted SCAPS-1D simulation tool, we systematically designed and optimized a novel device architecture consisting of Al/SnO_2:F/Bi_2S_3/$BaSi_2$/Ni. The primary objective is to enhance device performance by optimizing critical parameters such as layer thicknesses, carrier concentrations, bulk defect densities in each layer, interface defects, operating temperatures, and the influence of series and shunt resistance on overall efficiency.

The manuscript is organized as follows: Section 2 details the proposed device architecture; Section 3 presents theoretical approach to model the proposed solar device architecture; Section 4 presents an in-depth discussion of the obtained results; finally, Section 5 concludes with key insights drawn from this research endeavour.

II. Device Architecture

The $BaSi_2$-based thin-film solar cell, as depicted in Figure 1(a), features a multi-layered structure with the configuration Al/SnO_2:F/Bi_2S_3/$BaSi_2$/Ni. In this design, Fluorine-doped tin oxide (SnO_2:F) serves as the window layer in this design due to its high conductivity and optical transparency, followed by a bismuth trisulphide (Bi_2S_3) layer that functions as the electron transport layer (ETL), and finally the absorber layer barium disilicide ($BaSi_2$). The Al and Ni act as front and rear contacts, respectively. Light is illuminated from the SnO_2:F side, allowing the absorber layer to effectively collect incoming light.

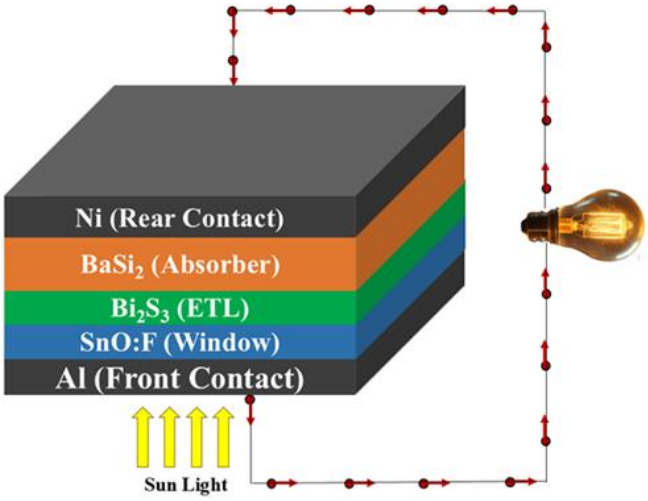

(a)

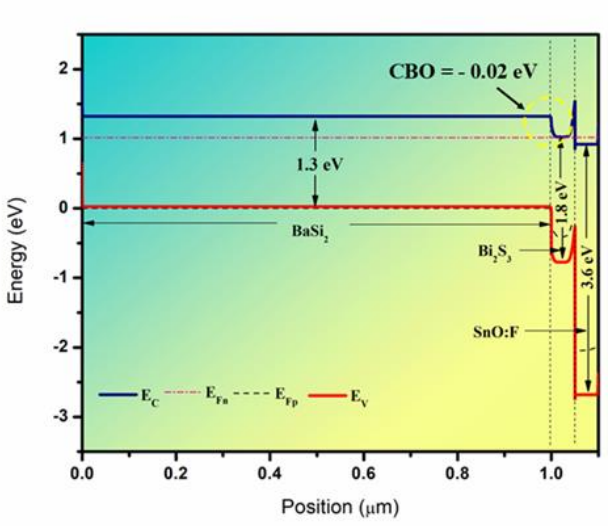

(b)

Figure 1 (a) The proposed device architecture (b) Band alignment diagram

Figure 1(b), illustrates the band diagram of the presented solar cell, crucial for comprehending the charge carrier dynamics and energy levels within the device. To ensure efficient electron extraction at the ETL-absorber interface, a minimum conduction band offset (CBO) is desired. The CBO can be calculated using the formula [25]:

$$CBO = \chi_{Absorber} - \chi_{ETL}$$

According to Table 1, n-Bi_2S_3 has an electron affinity (χ) of 3.32 eV, while p-$BaSi_2$ has an electron affinity (χ) of 3.30 eV. This yields a CBO of -0.02 eV, forming a favorable p-n heterojunction that facilitates effective electron extraction, as clearly indicated in Figure 1(b).

Further, lattice mismatch is another crucial parameter which significantly influences charge transport and overall device performance. It refers to the difference in lattice constants between two interfacing materials, which can result in undesirable band alignments and the formation of interfacial defects. These defects lead to increased carrier recombination, thereby reducing the efficiency of the photovoltaic device. Therefore, when designing a device, it is essential to consider a material which exhibits least lattice mismatch when interface. The degree of lattice mismatch (δ) can be determined using the following formula [23]

$$\delta = 2\,|a_s - a_e|/(a_s + a_e)$$

where a_s is the lattice constant of the substrate, and a_e is the lattice constant of the epitaxial thin film. For the Bi_2S_3/$BaSi_2$ interface, the lattice mismatch is calculated to be 4.4%, based on the lattice constants of $BaSi_2$ (11.55 Å) and Bi_2S_3 (11.13 Å). This relatively small mismatch facilitates the formation of a stable interface, promoting efficient charge transport and improved device performance.

The performance of the solar cell was simulated under standard test conditions (STC), which include a solar irradiance of 100 mW/cm² under AM 1.5G spectrum and a working temperature of 300 K. To mimic practical conditions, series and shunt resistances were set at 0.5 and 10^5 ohm/cm², respectively.

3. Theoretical framework and Modelling:

SCAPS-1D is a powerful one-dimensional simulation tool developed and modernized by the Department of Electronics and Information Systems at the University of Ghent in Belgium [23, 26-27]. It is widely used to analyze and optimize the performance of various semiconductor devices.

SCAPS-1D employs a numerical method, typically the finite difference method, to iteratively solve the set of equations that govern carrier transport, recombination, and electrostatic potential within a device architecture, thereby offering critical insights into device characteristics such as current-voltage (I-V) curves, spectral response, and efficiency.

Poisson's equation is a fundamental relation in electrostatics that connects charges to the

electrostatic potential and can be expressed as follows [23, 26-27]:

$$\nabla^2 \emptyset = -\frac{q}{\varepsilon_0 \varepsilon_r}\left[p - n + N_D^+ - N_A^- + \rho_p - \rho_n\right] \quad (1)$$

Here, each symbol has its unique meaning, for instance, ε_0 *and* ε_r represent vacuum and relative permittivity, $\emptyset$ is the electrostatic potential, q is the elementary charge, p *and* n are the concentration of holes and free electrons, N_D^+ *and* N_A^- denote the concentration of ionized donors and acceptors, and ρ_p *and* ρ_n are the distribution of holes and electrons.

The continuity equations for electrons and holes under steady-state conditions are given by [23, 26-27]:

$$\nabla \cdot J_n = q[-G_n + R_n] \quad (2)$$

$$\nabla \cdot J_p = q\,[G_p - R_p] \quad (3)$$

In the above equations, J_n *and* J_p refers to the electron and hole current density, R_n *and* R_p represent electron and hole net recombination rates per unit volume, and G_n *and* G_p are electron and hole generation rates per unit volume.

The transportation properties of electrons and holes are derived by [23, 26-27]:

$$J_n = -\frac{\mu_n n}{q} \nabla \cdot E_{F_n} \quad (4)$$

$$J_p = +\frac{\mu_p p}{q} \nabla \cdot E_{F_p} \quad (5)$$

The symbols μ_n *and* μ_p are for electron and hole mobilities. In contrast, E_{F_n} *and* E_{F_p} are the quasi-fermi levels for electrons and holes, respectively.

To accurately model a device using SCAPS-1D, it is essential to define the device geometry and material properties which are outlined in Table. 1 and 2. For Bi_2S_3/$BaSi_2$ interface, neutral defect was considered with single energy distribution. The interface defect density was varied from 10^{10} – 10^{18} cm^{-2}.

Table 1. Input parameters for various layers used in the SCAPS-1D simulation [19, 28, 29]

Parameters	SnO:F	Bi_2S_3	$BaSi_2$
Thickness (μm)	0.05	0.05*	1*
E_g (eV)	3.6	1.8	1.3
χ (eV)	4	3.32	3.30
ε_r	9	38	11.17
N_c (1/cm³)	2.2E+18	1.4E+19	2.6E+19
N_v (1/cm³)	1.8E+19	7.1E+16	2.0E+19
V_e (cm/s)	1E+07	1E+07	1E+07
V_h (cm/s)	1E+07	1E+07	1E+07
μ_e (cm²/V s)	100	32	820
μ_h (cm²/V s)	25	3	100
N_D (1/cm³)	1E+20	1E+19*	0
N_A (1/cm³)	0	0	5E+19*
Defect density type	Neutral	Single Donor	Single Donor
σ_e (cm²)	1E-19	1E-19	1E-19
σ_h (cm²)	1E-19	1E-19	1E-19
Energetic Distribution	Single	Uniform	Uniform
N_t (1/cm³)	1E+14	1E+14*	1E+14*

***Variable Parameters**

Table 2 Input parameters for metallic contacts

Parameters	Front contact (Al)	Rear Contact (Ni)
Work function (eV)	4.06	5.35
SRV of electrons (cm/s)	1E+05	1E+05
SRV of holes (cm/s)	1E+05	1E+05

III. RESULTS AND DISCUSSION

Figure 2 (a) illustrates the variation in performance parameters with BaSi2 thickness. It is noteworthy that with an increase in thickness, the open-circuit voltage (Voc), short-circuit current density (Jsc), and overall efficiency (η) exhibit a downward trend, whereas the fill factor (FF) demonstrates an upward trend. The fall in Voc is attributed to increased recombination rates in thicker absorber layers. Thicker absorber layers increase the path length for carriers generated deeper in the material, resulting in increased recombination prior to collection. This elevates the dark saturation current (J0), which in turn reduces Voc according to the equation [25]:

$$V_{oc} = \frac{kT}{q} \ln\left(\frac{J_{sc}}{J_0} + 1\right) \quad (6)$$

Jsc is determined by the number of photogenerated carriers and their effective collection at contacts. As the thickness of the $BaSi_2$ layer increases, the probability of recombination within the absorber layer also increases. This leads to a reduction in the number of charge carriers reaching the electrodes, thereby decreasing Jsc. The FF experiences a marginal enhancement in charge collection efficiency due to a reduction in series resistance, but it remains dominated by recombination losses affecting Voc and Jsc. Consequently, the overall efficiency diminishes with increased thickness, as enhanced recombination outweighs the benefits of light absorption and reduces the number of carriers reaching the contacts.

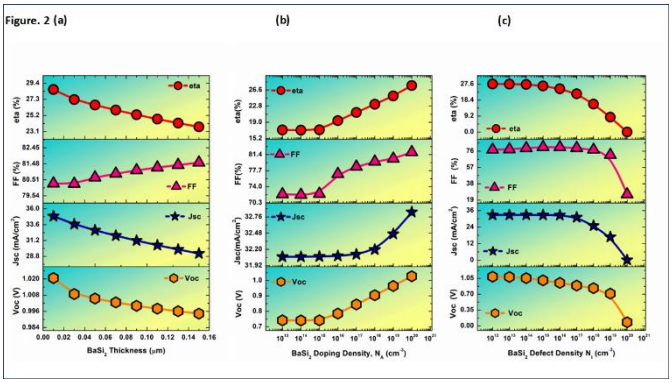

Figure 2 Variation of performance parameters of solar cell with respect to (a) BaSi2 Thickness (b) BaSi2 doping density and (c) Basi2 defect density

Figure 2 (b) shows the variation in performance parameters corresponding to the doping density of $BaSi_2$. The results obtained indicate that with an increase in doping density, the Voc shows an increasing trend. This enhancement can be ascribed to the reduction in recombination losses occurring within the absorber layer. Higher doping densities result in an increase in the quasi-Fermi level splitting, thus enhancing the Voc. Jsc shows a slight increase with higher doping density. This can be elucidated by the improved electric field within the depletion region, which enhances the separation and collection of photogenerated carriers. However, the increase is not as prominent as that observed in Voc, suggesting that variables such as optical absorption and carrier mobility also exert a considerable influence on Jsc. The FF shows a notable increase with higher doping levels. This improvement is due to the reduction in series resistance and the increase in shunt resistance as the doping density increases. Higher doping levels

improve the conductivity of the absorber layer, reducing series resistance, and enhancing overall device performance. This results in an improved quality of the IV curve, which in turn leads to a higher FF. η displays a significant increase with increasing doping density. This is a direct consequence of the combined improvements in Voc, Jsc, and FF. As higher doping enhances the electric field, reduces recombination, and improves carrier collection, the efficiency of the solar cell increases.

Figure 2 (c) represents the variation in performance parameters corresponding to the defect density of $BaSi_2$. From the figure, it is evident that Voc experiences a gradual decline as defect density increases. These defects create trap states that capture charge carriers, thereby reducing the potential barrier necessary for the carriers to contribute to the current. This reduced energy barrier directly results in a lower Voc, as the defect states promote recombination and decrease the voltage at which current generation stops. Jsc exhibits a consistent trend at lower defect densities, but it begins to decrease as the defect density surpasses ~10^{17} cm^{-3}. The reduction in Jsc is due to the increased probability of recombination occurring prior to the collection of charge carriers. As the defect density increases, more carriers recombine non-radiatively, thereby reducing the current. Similarly, FF remains nearly constant till defect density 10^{18} cm^{-3} beyond this threshold, it experiences a pronounced decline. Higher defect densities increase the series resistance and decrease the shunt resistance of the solar cells. These defects serve as recombination centers and traps, obstructing the movement of charge carriers and amplifying resistive losses, thus leading to a reduction in the FF. Lastly, the efficiency (η) mirrors the trend observed in Jsc and FF. It remains relatively stable at lower defect densities but decreases significantly beyond 10^{16} cm^{-3}. This trend can be attributed to the introduction of non-radiative recombination pathways at higher defect densities, which shorten the lifetime of charge carriers and diminish the overall collection efficiency. According to the Shockley-Read-Hall (SRH) recombination theory, the recombination rate increases with defect density, leading to shorter charge carrier lifetimes and reduced carrier collection efficiency. As a result, higher defect densities cause a significant degradation in performance, as reflected in the decline of Voc, Jsc, FF, and η.

Figure 3 (a) presents the variation of performance parameters as a function of Bi_2S_3 thickness. The decline in Voc with increasing Bi_2S_3 thickness can be attributed to inadequate charge transport and increased recombination losses. As the thickness increases, the resistance within the ETL rises, which impedes efficient electron extraction. The decrease in Jsc with increasing Bi_2S_3 thickness is closely linked to optical and electrical losses. A thicker ETL can act as a barrier to the efficient collection of photogenerated electrons, increasing the probability of recombination before they reach the external circuit. Furthermore, Thicker ETLs may block or scatter some of the incident light, reducing the amount of light reaching the absorber layer and thus limiting the generation of electron-hole pairs. Consequently, fewer charge carriers contribute to the photocurrent, leading to a reduction in Jsc. The initial increase in FF with a slight increase in Bi_2S_3 thickness can be attributed to improved charge separation and transport within the device, particularly if the thin ETL layer was previously insufficient for optimal electron extraction. A slightly thicker layer may improve the interface between the absorber and the ETL, reducing the series resistance and improving the alignment of energy levels. Nevertheless, the fill factor reaches a plateau when the thickness reaches a certain level, as further increases do not provide any additional benefits. Beyond this point, the effects of increased resistive losses due to the longer electron diffusion lengths and potential recombination become dominant, preventing further improvement in the fill

factor. As the thickness of the Bi_2S_3 layer increases, the distance that electrons must travel before being collected at the contact also increases. This leads to higher resistive losses due to increased series resistance, as electrons encounter more scattering events. Moreover, thicker ETL layers can also result in an increased likelihood of recombination before the charges are collected, thereby reducing the number of photogenerated carriers that contribute to the photocurrent. Consequently, the efficiency decreases as a result of diminished charge extraction efficiency and enhanced recombination.

Figure 3 (b) illustrates the variation of performance parameters as a function of Bi_2S_3 donor densities. The Voc initially exhibits a slight rise as the shallow donor density (N_D) increases, after which it stabilizes. This behaviour can be attributed to the increase in electron concentration in the conduction band as N_D increases, which in turn raises the Fermi level and leads to the observed increase in Voc. Jsc is largely constant up to a certain donor density (~10^{17} cm^{-3}), after which it declines noticeably as N_D continues to rise. At lower N_D, the constant Jsc can be explained by enhanced carrier generation and collection efficiency, as more free electrons are available to contribute to the photocurrent. However, beyond a critical doping level, recombination losses—especially Auger recombination—become more pronounced, leading to fewer collected charge carriers. This reduction in Jsc at higher N_D occurs as the depletion region narrows and increased recombination diminishes current collection. Meanwhile, the FF exhibits an upward trend as N_D increases. This is mostly owing to improved conductivity in the Bi_2S_3 layer, resulting from the higher concentration of free carriers (electrons) provided by the shallow donor states. The reduction in series resistance enhances the FF, compensating for the narrower depletion region. As a result, even at higher doping levels, the FF remains positively affected by the reduced resistive losses. Overall, the efficiency remains relatively constant, with a slight increase as N_D increases. This suggests that while doping density plays a role in influencing individual parameters like Voc, Jsc, and FF, its effect on the overall efficiency is limited within the analysed range.

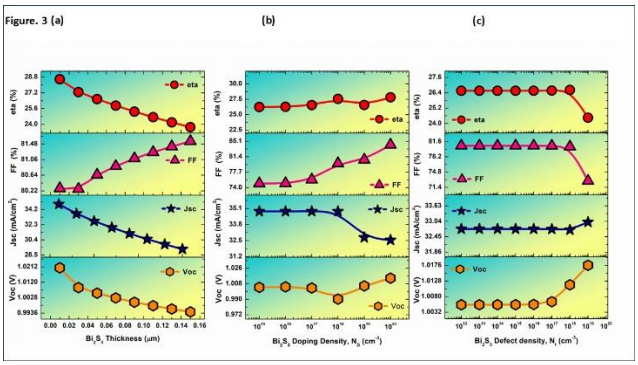

Figure 1 Variation of performance parameters of solar cell with respect to (a) Bi_2S_3 Thickness (b) Bi_2S_3 doping density and (c) Bi_2S_3 defect density

Figure 3 (c) display the variation of performance parameters as a function of Bi_2S_3 defect densities. At lower defect densities, the Voc remains relatively flat and it even exhibits a slight increase at higher defect densities. At lower defect densities, the recombination rates are low, and the quasi-Fermi level splitting remains unaffected, leading to stable Voc values. As defect density increases, more recombination centers are introduced, and one would expect Voc to decrease due to increased losses. However, in this case, the slight increase in Voc at higher defect densities may be explained by the shift in the built-in potential across the junction, which can occur as a result of changes in the carrier concentration profile due to increased doping or compensation by defects. The short-circuit current density remains stable over a broad range of defect densities but starts to decrease at very high defect densities. In the low to mid-range of defect densities, there is minimal impact on photogenerated carriers, and most of the carriers are still collected effectively, keeping Jsc nearly constant. However, as defect density increases significantly, the recombination rate increases in the bulk and at the junction, leading to a

loss of photogenerated carriers before they can be collected, thus reducing Jsc. η and FF remain nearly constant at lower defect densities (10^{12} to 10^{17} cm^{-3}). At these densities, the defects introduce a small number of recombination centers, implying that their influence on carrier recombination is limited. The charge carriers generated in the absorber can still be effectively collected, resulting in stable values for both efficiency and fill factor. However, as the defect density exceeds a critical threshold (around 10^{17} cm^{-3}), efficiency decreases in tandem with the FF since efficiency is a function of both FF and the other parameters. The sharp decline in efficiency and FF at higher defect densities can be attributed to the increased non-radiative recombination, which causes a significant loss in the photogenerated current.

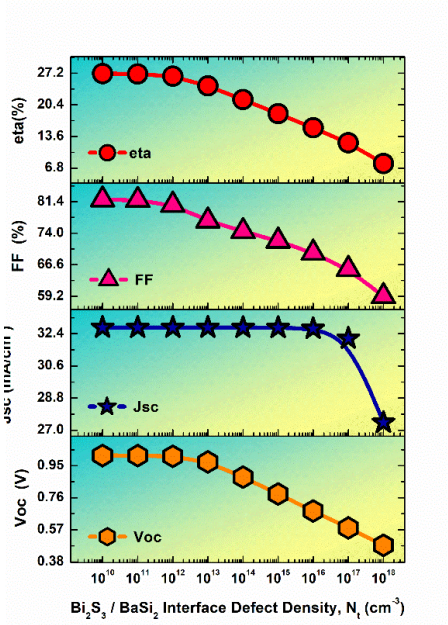

Figure 2 Variation of performance parameters of solar cell with respect to Bi_2S_3/$BaSi_2$ Interface defect density

Figure 4 shows the variation of performance parameters as a function of interface defect densities at Bi_2S_3/$BaSi_2$ interface. The monotonous decrease in Voc with increasing N_t can be explained by the increased recombination at defects, which reduces the effective built-in potential of the solar cell. Higher defect densities diminish the separation of charge carriers, thus lowering the maximum voltage achievable when no current flows. At low defect densities, electron-hole pair production remains effective, resulting in roughly constant Jsc values. However, as defect density increases, the sharp decline in Jsc occurs due to enhanced recombination of carriers before they can contribute to the current, leading to a significant reduction in the available current. The initial slight decrease in FF followed by a sharper decline as defect density increases indicates that while the device operates efficiently at low defect levels, the increase in defects leads to increased recombination losses and reduced voltage. This impacts the maximum power output, causing FF to drop more significantly at higher defect densities. The decline in efficiency with increasing interface defect density (N_t) can be attributed to increased recombination of charge carriers at defects. Higher defect densities create more sites for non-radiative recombination, reducing the number of charge carriers that contribute to the current, thus lowering efficiency.

Figure 5 (a) depicts the variation of performance parameters as a function of series resistance. It is evident from the figure that series resistance has a limited effect on open-circuit voltage because no current flows in this condition. However, there is a minor drop due to reduced carrier collection efficiency and recombination effects caused by the increased *Rs*. Jsc remains mostly constant, but it decreases slightly as Rs increases as Rs increases due to the non-ideal behaviors of the solar cell under operational conditions, such as increased recombination rates that could occur due to increased voltage drop across the resistance. Rs causes power loss in the form of heat, which reduces the overall power output. As Rs increases, more power is dissipated within the cell, leading to a sharp decline in both efficiency and fill factor. The higher *Rs* reduces the maximum power point, causing a significant drop in these parameters.

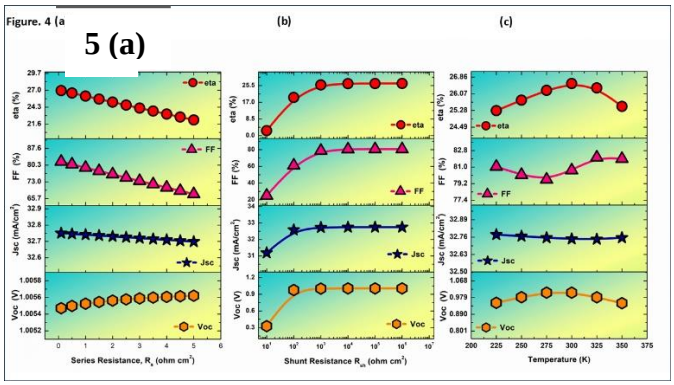

Figure 3 Variation of performance parameters of solar cell with respect to (a) Series Resistance (b) Shunt Resistance and (c) Temperature

Figure 5 (b) shows the variation of performance parameters as a function of shunt resistance. It is evident from the figure that at low Rsh, significant leakage currents flow through the shunt path, leading to power losses and a lower Voc. As Rsh increases, these leakage currents decrease, allowing Voc to rise rapidly. Beyond a certain value, the leakage becomes negligible, causing Voc to plateau since further increases in Rsh no longer influence the junction potential.

Jsc experiences only a minor increase with rising Rsh because low Rsh causes current loss through shunt pathways, which reduces Jsc marginally. As Rsh increases, these losses diminish, but the current through the main path is already maximized, leading to minimal change at higher Rsh values. The FF and efficiency follow similar trends, with a sharp increase at low Rsh as shunt losses decrease. As Rsh continues to rise, FF and efficiency plateau when leakage becomes insignificant. Beyond this threshold, further increases in Rsh have minimal impact, as other factors like series resistance and material properties dominate.

Figure 5 (c) shows the variation of performance parameters as a function of temperature. The figure illustrates that Voc decreases as the temperature rises. This behaviour is consistent with the well-established link between Voc and temperature described by equation (6). As temperature rises, the reverse saturation current J0 grows exponentially, resulting in a drop in Voc. This trend is typical for most solar cells since increasing temperature increases recombination rates, lowering the effective carrier concentration available for voltage generation. Besides recombination, another factor influencing Voc is the temperature dependency of the bandgap, which normally decreases with rising temperature, contributing to the drop of Voc. The drop in Voc at higher temperatures, as seen in the graph, is therefore expected. Jsc remains nearly constant with temperature. This consistency is explained by the fact that temperature changes may cause minor variations in photon absorption and carrier mobilities. In other words, the light absorption and generation of electron-hole pairs in the $BaSi_2$ layer are relatively unaffected by temperature in the range studied. Thus, temperature-induced recombination effects have a smaller effect on Jsc. The FF shows a relatively weak, but observable, temperature dependence. The FF is influenced by both series resistance and recombination mechanisms in the device. Initially, there is a small dip observed in FF, followed by an increase, and then it remains almost constant at higher temperatures. The small dip in FF at lower temperatures can indeed be due to increased series resistance as carrier mobility is reduced at these temperatures. As the temperature increases, the carrier mobility improves due to thermal excitation, resulting in lower resistive losses, which may explain the improvement in FF. However, as temperatures rise further, increased recombination effects start to balance out any mobility gains, leading to the nearly constant FF observed at higher temperatures. The efficiency shows a non-linear behaviour as a function of temperature, initially increasing with temperature up to a peak value and then decreasing beyond a specific threshold. At lower temperatures, the rise in efficiency is due to improvements in Voc and FF, as seen in their respective graphs. However, at a certain

temperature (~325 K in this case), the efficiency begins to drop, perhaps due to the reduction in Voc. This drop in Voc is directly linked to the thermal excitation of charge carriers and increased recombination.

Table 3 Comparative of Solar Cell Performance – Previously Reported Configurations vs. Proposed Configuration

Sr. No.	Device Structure	V_{oc} (V)	J_{sc} (mA/cm²)	FF (%)	η (%)	Ref.
1	p-$BaSi_2$/n-c-Si	0.44	37.00	59.70	9.80	14
2	p-$BaSi_2$/n-Si	0.54	32.80	51.90	9.25	20
3	FTO/Zn (O, S)/$BaSi_2$/Ni	0.60	34.40	81.96	17.00	20
4	FTO/SnS_2/$BaSi_2$/Ni	0.62	34.45	82.07	17.10	20
5	FTO/WS_2/$BaSi_2$/Ni	0.76	35.23	82.40	22.20	20
6	Al/SnO:F/CdS/$BaSi_2$/Cu	1.06	34.23	72.14	26.32	19
7	Al/SnO:F/Bi_2S_3/$BaSi_2$/Ni	1.00	32.74	80.65	26.56	*PW

**PW indicates present work*

IV.CONCLUSION

The present manuscript effectively demonstrates the suitability of Bi_2S_3 as an electron transport layer (ETL) in $BaSi_2$-based thin-film solar cells. With a low lattice mismatch of 4.4% and a conduction band offset (CBO) of -0.02 eV with $BaSi_2$, Bi_2S_3 promotes favourable band alignment, facilitating efficient charge carrier transport and enhancing device performance. The proposed novel solar design is further evaluated using the globally recognized SCAPS-1D tool, optimizing various physical and parasitic parameters to achieve optimal performance. The resulting performance metrics, as shown in Table 3, exhibit notable improvements compared to recent theoretical and experimental reports on similar solar cell configurations. Overall, this research enhances the understanding of optimizing p-$BaSi_2$/n-Bi_2S_3 heterojunction solar cells, thereby expanding their potential applications in future photovoltaic and optoelectronic technologies.

Acknowledgments:
The author wishes to acknowledge Dr. Marc Burgelman, University of Gent, Belgium, for the SCAPS-1D simulation software.

Data Availability: Provided in Manuscript.

Conflict of Interest: There is no conflict of interest.

V. REFERENCES

[1]. M. Okil, M. S. Salem, T. M. Abdolkader, and A. Shaker, From Crystalline to Low-cost Silicon-based Solar Cells: a Review, Silicon 2021 14:5, 14(5), 1895-1911 (2021).

[2]. A.K. Sharma, R. Kumar, P. K. Jha, M. Kumar, N. K. Chourasia, and R. K. Chourasia, Bulk

Parameters Effect and Comparative Performance Analysis of p-Si/n-CdS/ALD-ZnO Solar Cell, Silicon, 15(15), 6497-6508 (2023).

[3]. A.K. Sharma, A. Srivastava, P. K. Jha, R. Kumar, M. Kumar, P. K. Kulriya, N. K. Chourasia, and R. K. Chourasia, Bulk/Interface Defects Engineering and Comparative Performance Analysis of p-Si/n-CdS/ALD-ZnO Heterojunction Solar Cell, Energy Technology, 11(8), 2300169 (2023).

[4]. Sharma, A. K., Srivastava, A., Jha, P. K., Sangani, K., Chourasia, N. K., & Chourasia, R. K. Signal Components and Impedance Spectroscopy of Potential p-Si/n-CdS/ALD-ZnO Solar Cells: EIS and SCAPS-1D Treatments. Advanced Theory and Simulations, 2400688, (2024).

[5]. Smets, A., Jäger, K., Isabella, O., Van Swaaij, R., & Zeman, M., Solar Energy: The physics and engineering of photovoltaic conversion, technologies and systems, Bloomsbury Publishing, (2016).

[6]. Suemasu, T., Exploring the possibility of semiconducting BaSi2 for thin-film solar cell applications, Japanese Journal of Applied Physics, 54(7S2), (2015).

[7]. Morita, K., Inomata, Y., & Suemasu, T., Optical and electrical properties of semiconducting BaSi2 thin films on Si substrates grown by molecular beam epitaxy, Thin Solid Films, 508(1-2), 363-366, (2006).

[8]. Migas, D. B., Shaposhnikov, V. L., & Borisenko, V. E., Isostructural BaSi2, BaGe2 and SrGe2: electronic and optical properties. physica status solidi (b), 244(7), 2611-2618, (2007).

[9]. Toh, K., Saito, T., & Suemasu, T., Optical absorption properties of BaSi2 epitaxial films grown on a transparent silicon-on-insulator substrate using molecular beam epitaxy. Japanese Journal of Applied Physics, 50(6R), 068001, (2011).

[10]. Kumar, M., Umezawa, N., & Imai, M., (Sr, Ba)(Si, Ge) 2 for thin-film solar-cell applications: first-principles study. Journal of Applied Physics, 115(20), (2014).

[11]. Baba, M., Watanabe, K., Hara, K. O., Toko, K., Sekiguchi, T., Usami, N., & Suemasu, T., Evaluation of minority carrier diffusion length of undoped n-BaSi2 epitaxial thin films on Si (001) substrates by electron-beam-induced-current technique. Japanese Journal of Applied Physics, 53(7), 078004, (2014).

[12]. Hara, K. O., Usami, N., Nakamura, K., Takabe, R., Baba, M., Toko, K., & Suemasu, T., Determination of bulk minority-carrier lifetime in BaSi2 earth-abundant absorber films by utilizing a drastic enhancement of carrier lifetime by post-growth annealing. Applied Physics Express, 6(11), 112302, (2013).

[13]. Baba, M., Tsurekawa, S., Watanabe, K., Du, W., Toko, K., Hara, K. O., ... & Suemasu, T., Evaluation of potential variations around grain boundaries in BaSi2 epitaxial films by Kelvin probe force microscopy. Applied physics letters, 103(14), (2013).

[14]. Tsukahara, D., Yachi, S., Takeuchi, H., Takabe, R., Du, W., Baba, M., ... & Suemasu, T., p-BaSi2/n-Si heterojunction solar cells with conversion efficiency reaching 9.0%. Applied physics letters, 108(15), (2016).

[15]. Yachi, S., Takabe, R., Takeuchi, H., Toko, K., & Suemasu, T., Effect of amorphous Si capping layer on the hole transport properties of BaSi2 and improved conversion efficiency approaching 10% in p-BaSi2/n-Si solar cells. Applied Physics Letters, 109(7), (2016).

[16]. Deng, Q., Chen, H., Liao, H., Chen, L., Wang, G., Wang, S., & Shen, Y., Numerical simulation and optimization of Si/BaSi2 heterojunction and BaSi2 homojunction solar cells. Journal of Physics D: Applied Physics, 52(7), 075501, (2018).

[17]. Vismara, R., Isabella, O., & Zeman, M., Organometallic halide perovskite/barium di-silicide thin-film double-junction solar cells. In Photonics for Solar Energy Systems VI (Vol. 9898, pp. 54-62). SPIE, 2016.

[18]. Chen, L., Chen, H., Deng, Q., Wang, G., & Wang, S., Numerical simulation of planar BaSi2 based Schottky junction solar cells toward high efficiency. Solid-State Electronics, 149, 46-51, (2018).

[19]. Moon, M. M. A., Ali, M. H., Rahman, M. F., Kuddus, A., Hossain, J., & Ismail, A. B. M., Investigation of thin-film p-BaSi2/n-CdS heterostructure towards semiconducting silicide based high efficiency solar cell. Physica Scripta, 95(3), 035506, (2020).

[20]. Rahman, M. F., Shanto, M. A. B., Ali, M. A., Marasamy, L., Benami, A., Chaudhry, A. R., & Irfan, A., A new exploration of the impact of different wide-bandgap S-chalcogenides Electron Transport Layers (ETL) on the performance of BaSi2-based solar cells. Emergent Materials, 1-17, (2024).

[21]. Lim, E. L., Yap, C. C., Jumali, M. H. H., Teridi, M. A. M., & Teh, C. H., Inverted organic solar cells integrated with room temperature solution-processed bismuth sulfide electron selective layer. Solar Energy, 157, 1108-1113, (2017).

[22]. Liang, Z., Zhang, Q., Jiang, L., & Cao, G., ZnO cathode buffer layers for inverted polymer solar cells. Energy & Environmental Science, 8(12), 3442-3476, (2015).

[23]. Pandya, A., Sharma, A. K., Bhatt, M., Jha, P. K., Sangani, K., Chourasia, N. K., & Chourasia, R. K., A synergy of Cr2O3 with eco-friendly and thermally stable CsSnCl3 perovskite for solar energy storage: Density functional theory and SCAPS-1D analysis. Energy Storage, 6(5), e70001, (2024).

[24]. Moreno-García, H., Messina, S., Calixto-Rodriguez, M., & Martínez, H., Physical properties of chemically deposited Bi2S3 thin films using two post-deposition treatments. Applied surface science, 311, 729-733, (2014).

[25]. Rahman, M. M., Ali, M. H., Haque, M. D., & Islam, A. Z. M. T., Numerical modeling and extensive analysis of an extremely efficient RbGeI 3-based perovskite solar cell by incorporating a variety of ETL and HTL materials to enhance PV performance. Energy Advances, 3(9), 2377-2398, (2024).

[26]. Burgelman, M., Decock, K., Niemegeers, A., Verschraegen, J. & Degrave, S. SCAPS manual. in (2023).

[27]. Shukla, R., Kumar, R. R. & Pandey, S. K. Theoretical Study of Charge Carrier Lifetime and Recombination on the Performance of Eco-Friendly Perovskite Solar Cell. IEEE Trans Electron Devices 68, 3446–3452 (2021).

[28]. Vincent Mercy, E. N., Srinivasan, D., & Marasamy, L., Emerging BaZrS3 and Ba (Zr, Ti) S3 chalcogenide perovskite solar cells: A numerical approach toward device engineering and unlocking efficiency. ACS omega, 9(4), 4359-4376, (2024).

[29]. Pineda, E., Nicho, M. E., Nair, P. K., & Hu, H., Optoelectronic properties of chemically deposited Bi2S3 thin films and the photovoltaic performance of Bi2S3/P3OT solar cells. Solar Energy, 86(4), 1017-1022, (2012).